Check for updates

The smallest superatom Au$_4$(PPh$_3$)$_4$I$_2$ with two free electrons: synthesis, structure analysis, and electrocatalytic conversion of CO$_2$ to CO†

Cheng Zhang, Mei Ding, Yonggang Ren, Along Ma, Zhengmao Yin,*
Xiaoshuang Ma [ID] * and Shuxin Wang [ID] *

Atomically precise metal nanoclusters (NCs) have emerged as a new class of ultrasmall nanoparticles with both free valence electrons and precise structures (from the metal core to the organic ligand shell) and provide great opportunities to understand the relationship between their structures and properties, such as electrocatalytic CO$_2$ reduction reaction (eCO$_2$RR) performance, at the atomic level. Herein, we report the synthesis and the overall structure of the phosphine and iodine co-protected Au$_4$(PPh$_3$)$_4$I$_2$ (Au$_4$) NC, which is the smallest multinuclear Au superatom with two free e$^-$ reported so far. Single-crystal X-ray diffraction reveals a tetrahedral Au$_4$ core stabilized by four phosphines and two iodides. Interestingly, the Au$_4$ NC exhibits much higher catalytic selectivity for CO (FE$_{CO}$: > 60%) at more positive potentials (from −0.6 to −0.7 V *vs.* RHE) than Au$_{11}$(PPh$_3$)$_7$I$_3$ (FE$_{CO}$: < 60%), a larger 8 e$^-$ superatom, and Au(ı)PPh$_3$Cl complex; whereas the hydrogen evolution reaction (HER) dominates the electrocatalysis when the potential becomes more negative (FE$_{H_2}$ of Au$_4$ = 85.8% at −1.2 V *vs.* RHE). Structural and electronic analyses reveal that the Au$_4$ tetrahedron becomes unstable at more negative reduction potentials, resulting in decomposition and aggregation, and consequently the decay in catalytic performance of Au based catalysts towards the eCO$_2$RR.

Introduction

The electrochemical CO$_2$ reduction reaction (eCO$_2$RR) can be regarded as an efficient method to convert CO$_2$ into a variety of high-value chemicals and fuels using electricity generated from renewable energy sources such as solar, wind, and tidal energy.[1–5] Due to the chemical inertness of CO$_2$, reducing CO$_2$ to high value-added chemicals requires sufficient activation energy to break C–O bonds. At present, the development of efficient catalysts to reduce activation energy and improve CO$_2$ conversion efficiency has become a research hotspot in this field, and remarkable results have been achieved.[6–10] However, the unclear structure–property relationship limits our deep understanding of eCO$_2$RR catalytic mechanisms at the atomic level.

Atomically precise metal nanoclusters (NCs) protected by ligands have attracted lots of interest for their unique properties and precise structures.[11,12] And NCs can be considered as an ideal model catalyst widely employed in the study of the catalytic mechanism of the eCO$_2$RR. For instance, the Jin group

systematically studied the influence of the Au NCs on their eCO$_2$RR properties such as the shape effect,[13] ligand effect,[14] and doping effect.[15,16] Subsequently, many studies have been devoted to the accurate identification of catalytically active sites of gold nanoclusters.[17,18] In 2021, the Lee group finally determined that the catalytic active site was the demercaptan gold atom at the interface through different sizes of Au$_{25}$, Au$_{38}$, and Au$_{144}$ NCs, and found a positive correlation between catalytic activity and cluster size.[19] The Wang group reported Au$_{28}$ and Au$_{55}$ NCs, showing high selectivity for CO (FE$_{CO}$ > 90%).[20,21] The Wu group introduced Cd to capture CO$_2$ at the interface of gold nanoclusters, forming a Cd–O–C(OH)–Au structure, which can effectively inhibit the competitive hydrogen evolution reaction (HER).[22] Zhu and co-workers found that C–S bond breaking on partial partitions makes it easier for open S sites to bind CO$_2$ to form catalytically active sites.[23] Recently, Zhu found that monomer Au$_{24}$Au$_{20}$ with a superatomic electronic configuration has better eCO$_2$RR catalytic reaction activity than dimer Au$_{43}$Ag$_{38}$ nanoclusters.[24] However, the relationship between the eCO$_2$RR performance and the size of Au NCs is still unclear. We are trying to push the limit and produce the smallest Au NC to answer the question. Moreover, few studies have been reported to explain the decay of eCO$_2$RR catalytic performance for Au NC-based catalysts at negative reduction potentials.

In this work, we report the synthesis, structure analysis and electroreduction performance of a novel Au$_4$(PPh$_3$)$_4$I$_2$ (**Au$_4$** hereafter) cluster with two free electrons, which is the smallest

College of Materials Science and Engineering, Qingdao University of Science and Technology, Qingdao 266042, Shandong, P. R. China. E-mail: yzm198752@163.com; xiaoshuang_Ma@qust.edu.cn; shuxin_wang@qust.edu.cn

cluster with free electrons reported so far. This structure is determined by single-crystal X-ray diffraction (SC-XRD). Furthermore, for comparison, $Au_{11}(PPh_3)_7I_3$ (**Au₁₁** hereafter) and the Au(I) complex (**Au(I)P** hereafter) were prepared to explore the structure and electron effects of clusters on the eCO₂RR. The three catalysts exhibited drastically different catalytic performances toward the eCO₂RR, which is not simply related to the size of the clusters. This work will provide guidance for the rational design of the Au-based catalysts for the eCO₂RR.

Experimental

Chemicals

All chemicals are of commercial grade and were used without further purification. Hydrogen tetrachloroaurate tetrahydrate ($HAuCl_4 \cdot 4H_2O$, 99.95%), triphenylphosphine (PPh₃, 98%), ethanol (HPLC grade, 99.9%), sodium hexafluoroantimonate ($NaSbF_6$, 99%), tetra-*n*-octylammonium bromide (TOAB, 98%), methylene chloride (CH_2Cl_2, HPLC grade, 99.9%), hexane (HPLC grade, 99.9%), sodium borohydride ($NaBH_4$, 99.99%), methanol (HPLC grade, 99.9%), ethyl ether (HPLC grade, 99.9%), *n*-pentane (HPLC grade, 99.9%), silver nitrate ($AgNO_3$, 99.9%), and sodium iodide (NaI, 99.9%). We purchased ultrapure water from Wahaha Co. Ltd. We cleaned all glassware with aqua regia (3 : 1 mix of hydrochloric acid and nitric acid), rinsed it with ultrapure water, and dried it before use.

Synthesis of the Au(I)(PPh₃)Cl complex (Au(I)P)

The Au complex was prepared according to a reported protocol with some minor modifications.[25] In a typical synthesis, $HAuCl_4 \cdot 3H_2O$ (500 mg, 1.21 mmol) was first dissolved in 35 mL of deaerated EtOH in a 100 mL round-bottom flask. Subsequently, PPh₃ (350 mg, 1.34 mmol) dissolved in 40 mL of deaerated EtOH was injected into the above solution under vigorous stirring, and white precipitates formed immediately. After 30 min, the white precipitates were filtered, washed with diethyl ether three times, and finally dissolved in CH_2Cl_2. Excess *n*-pentane was added dropwise to recrystallize the product to obtain white needle crystals of Au(PPh₃)Cl.

Synthesis of the Au(I)(PPh₃)NO₃ complex

Au(PPh₃)NO₃ was obtained by the counterion exchange reaction. Briefly, $AgNO_3$ (169.8 mg, 1 mmol) was dissolved in 10 mL MeOH and added to Au(PPh₃)Cl (446 mg, 0.9 mmol) dissolved in 50 mL CH_2Cl_2, and white precipitates AgCl formed immediately. After vigorous stirring for about 10 min, the mixture was centrifuged to remove AgCl, and the solvent organic phase was removed through rotary evaporation. The residual solid was washed with methanol several times to obtain white solids of Au(PPh₃)NO₃.

Synthesis of Au₄(PPh₃)₄I₂ nanoclusters (Au₄)

Au(PPh₃)NO₃ (25 mg, 0.05 mmol), and NaI (37.5 mg, 0.25 mmol) was added to 6 mL mixed solution of MeOH and CH_2Cl_2 (v : v = 1 : 2) with vigorous stirring. After about 20 min, $NaSbF_6$

(17.6 mg, 0.068 mmol) was added and stirred for 15 min. A freshly prepared $NaBH_4$ solution (2 mg in 4 mL of ice methanol) was added directly with vigorous stirring. The color changed from colorless to pale brown and finally to dark brown. After aging for 48 h, the solvent in the organic phase was removed through rotary evaporation, and then the product was washed with *n*-hexane three times and dissolved in CH_2Cl_2. After diffusion of *n*-hexane into CH_2Cl_2 at room temperature for about one week, orange-red crystals of $Au_4(PPh_3)_4I_2$ were obtained (yield: *ca.* 15% based on the Au atom).

Synthesis of Au₁₁(PPh₃)₇I₃ nanoclusters (Au₁₁)

$Au_{11}(PPh_3)_7I_3$ was synthesized according to the method described in the literature with slight modifications.[26] To a clean round-bottomed flask was added $HAuCl_4 \cdot 4H_2O$ (78 mg, 0.19 mmol), toluene (10 mL), TOAB (200 mg, 0.36 mmol), and stirred at room temperature for 1 hour until the color of the solution gradually deepened. After the gold salt was transferred from the aqueous phase to the organic layer, the water layer was removed by suction or centrifugation. The red organic layer was collected in a new round-bottomed flask, and NaI (5 mg, 0.033 mmol) was added, and stirred for 20 min. With intense agitation, PPh₃ (210 mg, 0.8 mmol) was added. The liquid changed from bright red to colorless, indicating the formation of the Au complex. After 20 min, $NaBH_4$ (90 mg, 2.38 mmol) ice water solution (5 mL) was added, stirred and aged for 24 h at room temperature. The color of the solution changed from colorless to brownish red. The reaction mixture was centrifuged to remove the water layer, and the crude product obtained after evaporation and drying was washed several times with *n*-hexane (30 mL) to remove impurities and obtain black precipitate. A single crystal **Au₁₁** NC was obtained by a stratified method. 2 mg of the product was dissolved with CH_2Cl_2 (2 mL), and was centrifuged to remove insoluble impurities, and then the black solution was layered with *n*-hexane (5 mL). After three days red crystals were obtained. The yield of **Au₁₁** is *ca.* 50% (based on the Au atom).

X-ray crystallography

The data collections for single crystal X-ray diffraction were carried out on a STOE Stradivari diffractometer at 150 K, using Mo Kα radiation ($\lambda = 0.71073$ Å). Data reductions and absorption corrections were performed using the X-Area. The structure was solved by intrinsic phasing and refined with full-matrix least squares on F^2 using the SHELXTL software package. All non-hydrogen atoms were refined anisotropically, and all the hydrogen atoms were set in geometrically calculated positions and refined isotropically using a riding model. Detailed crystal data and structure refinements for the cluster are given in Table S1.† CCDC 2251680 for $Au_4(PPh_3)I_2$ contains the ESI crystallographic data for this paper. These data are provided free of charge by the Cambridge Crystallographic Data Centre.

Electrochemical measurements

The catalyst sample was prepared by loading three as-prepared NCs on acidic multi-walled carbon nanotubes (CNTs) with

a mass ratio of 1 (5 mg NCs and 5 mg CNTs). The catalyst ink was obtained by dispersing the sample in isopropyl alcohol and sonicating for 5 min. Then, 1 mL of the catalyst suspension and 10 μL of Nafion (5 wt%) were mixed uniformly to form the final catalyst ink. Next, 40 μL of the catalyst ink was drop-cast onto a carbon cloth (1.0 × 1.0 cm^2) and dried at room temperature to make the working electrode. All electrochemical measurements were performed in a custom gas-tight H-cell with two compartments separated by a Nafion 117 membrane. Each compartment contained 25 mL of electrolyte (0.5 M KHCO$_3$: pH = 7.2 when saturated with CO$_2$ and pH = 8.8 when saturated with N$_2$) with 15 mL headspace. The electrochemical measurements were conducted on an electrochemical workstation (CHI 760E) with a Pt sheet as the counter electrode and an Ag/AgCl electrode (KCl saturated) as the reference electrode. All the potentials were calibrated to a reversible hydrogen electrode (RHE) according to the Nernst equation:

$$R(\text{RHE}) = E(\text{Ag/AgCl}) + 0.059 \times \text{pH} + 0.21 \quad (1)$$

The gas flow from the cathode chamber was directed into a gas chromatograph (GC3900Plus, RUI NENG) to identify and quantify the gaseous products. The GC was purged for 30 min with an average rate of 10 mL min^{-1} (at room temperature and ambient pressure) before the test. The GC was equipped with a thermal conductivity detector (TCD) for H$_2$ detection and a flame ionization detector (FID) for hydrocarbon detection. A methanizer (Agilent) was connected to the FID for CO detection. High-purity argon (99.9999%) was used as the carrier gas for all compartments of the GC. The faradaic efficiency (FE$_X$) and the corresponding partial current density (j_X) of X (X = CO or H$_2$) were calculated as follows:

$$\text{FE}_X = \frac{(N_i \times n \times F)}{Q_t} \quad (2)$$

$$j_X = \frac{\text{FE}_X \times Q_t}{t \times \text{area}} \quad (3)$$

where Q_t = total charge consumed in the electrochemical reaction, N_i = the number of moles of the product (measured using the GC), n = the number of electrons transferred in the elementary reaction (n is 2 for CO and H$_2$), F = the Faraday constant (96 485 C mol^{-1}), t = reaction time (s), and area = the geometric area of the electrode (1 cm^2).

The electrochemically active surface area (ECSA) of the catalyst was obtained via the linear fit of the corresponding current density with respect to the scan rate (Fig. S5†). The results indicated that the double layer capacitance of the electrode (C_{dI}) for Au(I)P, Au$_4$, and Au$_{11}$ was 0.648, 1.154, and 0.805 mF, respectively. The ECSA was calculated using the following formula:

$$\text{ESCA} = \frac{C_{dI}}{C_S} \quad (4)$$

where C_S is the specific capacitance of the sample or capacitance of an atomically smooth planar surface of the material per unit area under identical electrolyte conditions. And the average C_S value of 0.04 mF cm^{-2} for an ideal flat surface of the metal

catalyst in alkaline solution reported by McCrory was chosen for the ECSA evaluation.[27]

To evaluate catalyst stability, after the eCO$_2$RR, the samples were rinsed with CH$_2$Cl$_2$ from working electrodes and collected for characterization with UV-vis absorbance.

Results and discussion

Preparation and structure analysis of Au$_4$ and Au$_{11}$ NCs

Au$_4$(PPh$_3$)I$_2$ was first prepared by following a modified one-pot method (see experimental details). Briefly, in the presence of NaI and NaSbF$_6$, Au(I)(PPh$_3$)NO$_3$ were reduced by NaBH$_4$ in the mixed solvent of dichloromethane and methanol. The reaction was aged for two days during which the solution gradually changed from colorless to pale brown, and finally to dark brown. An orange-red block crystal was obtained by diffusing *n*-hexane into the dichloromethane solution containing the crude product. Subsequently, Au$_{11}$(PPh$_3$)$_7$I$_3$ with eight electrons was prepared by following the previously reported work to compare eCO$_2$RR catalytic performance with **Au$_4$**.

First, we compared the optical absorbance properties of **Au$_4$** and **Au$_{11}$**. For **Au$_4$**, as shown in Fig. 1a and c, there is only one prominent peak at 422 nm (2.94 eV). The energy bandgap derived from the absorbance spectrum is 2.51 eV. For **Au$_{11}$**, as presented in Fig. 1b and d, there are also one prominent peak at 419 nm (2.96 eV), and two weak shoulders at 300 nm (4.13 eV) and 315 nm (3.94 eV), while the energy bandgap of 1.88 eV agree well with the previously reported work.[26] Furthermore, one week stability of **Au$_4$** and **Au$_{11}$** in liquid state at room temperature was tested (Fig. S1†). It exhibits varying degrees of absorbance reduction, indicating that the stability of two clusters decreased due to structural collapse, while the deterioration rate of **Au$_4$** is significantly faster than that of **Au$_{11}$**. It is concluded that the stability of **Au$_4$** is relatively poor compared to that of **Au$_{11}$** at room temperature.
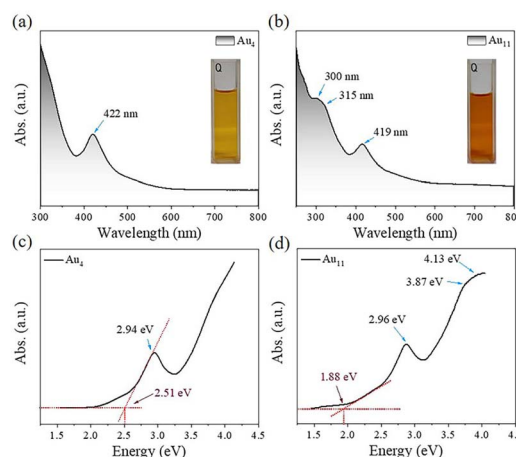

Fig. 1 The optical absorbance properties of two clusters. (a and b) UV-vis absorbance spectra and (c and d) the spectra plotted in the energy axis of Au$_4$ and Au$_{11}$ in CH$_2$Cl$_2$, respectively. Insets are the photos of Au$_4$ and Au$_{11}$ in CH$_2$Cl$_2$.
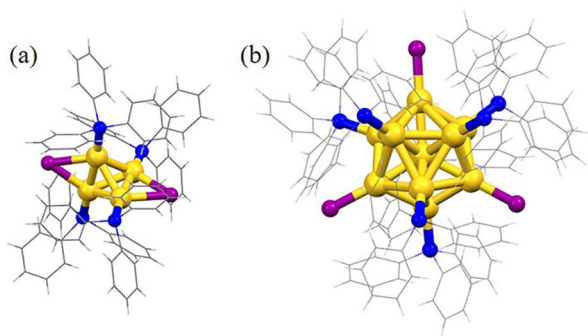
Fig. 2 Structural analysis of $Au_4(PPh_3)_4I_2$ and $Au_{11}(PPh_3)_7I_3$. Overall structure of monocationic (a) **Au₄** and (b) **Au₁₁**, respectively (color labels: yellow = Au, blue = P, grey = C, purple = I and white = H).

Subsequently, the atomic packing structure of $Au_4(PPh_3)_4I_2$ was examined using single crystal X-ray diffraction (SC-XRD). As illustrated in Fig. S2,† **Au₄** crystallizes in the space group $C2/c$ in the monoclinic crystal system, and each unit cell has no counterion, indicating that **Au₄** is electrically neutral. Therefore, $Au_4(PPh_3)_4I_2$ is a superatom containing two free electrons ($N = 4 - 2 - 0 = 2$). More detailed structural parameters are summarized in Table S1.† The comparison of overall structures of **Au₄** and **Au₁₁** is shown in Fig. 2. **Au₄** consists of a tetrahedral structure composed of four gold atoms, each of which is coordinated with one PPh₃ ligand (Fig. 2a). In addition, there are two iodine atoms, each of which forms a triangle with two gold atoms via σ bonding. This triangle, together with the PPh₃ ligands connected to the gold atoms, that is, two staple motifs and two iodine atoms together form **Au₄**. Along the line connecting the two iodine atoms as the axis, half of the cluster structure, that is, one staple motif, rotates 90° clockwise along the axis and overlaps with the projection of the other half of the staple motif. The bond lengths of Au–P are 2.282 and 2.292 Å, the bond lengths of Au–I are 2.898 and 2.972 Å, and the bond lengths of the adjacent Au–Au are 2.65, 2.74, and 2.83 Å (Fig. S3 and Table S2†). Furthermore, the structure of $Au_{11}(PPh_3)_7I_3$ consists of an **Au₁₁** core and seven PPh₃ ligands in the ligand shell (Fig. 2b). The remaining three gold atoms are bonded to iodine atoms, and the three iodine atoms form an approximate equilateral triangle with the center of mass located at the core gold atom. Ten of the eleven gold atoms form an incomplete icosahedral structure (missing one vertex and one edge gold atom), with only ten triangular faces and three non-planar quadrilateral faces. The remaining gold atom is located at the center of this incomplete icosahedral structure. The gold core can be viewed as consisting of a ring with four gold atoms and a ring with five gold atoms, as well as a gold atom located at the center of the pentagon and one at the top. The crystal belongs to the $P2_1/n$ space group (Fig. S3†). The Au–P bond length is between 2.271 and 2.297 Å, the Au–I bond length is between 2.595 and 2.609 Å, and the length of adjacent Au–Au bonds is between 2.608 and 3.109 Å (Fig. S3 and Table S2†). Moreover, the tetrahedron composed of four gold atoms is the smallest subunit for the structural evolution of Au nanoclusters.[28]

Electrocatalytic CO₂ reduction performance of the three catalysts

To evaluate the catalytic performance of cluster catalysts, the electrochemical CO₂ reduction reaction (eCO₂RR) was conducted. Given the abundant surface defects and functional groups of acidic multi-walled carbon nanotubes (CNTs), the two clusters and the Au(ı)PPh₃I complex (**Au(ı)P**) were deposited onto CNTs with 50% wt. loading to form the **Au(ı)P/CNT**, **Au₄/CNT** and **Au₁₁/CNT** electrocatalysts. By using gas chromatography (GC), it was discovered that CO and H₂ were the only two gaseous products compared to the reversible hydrogen electrode (RHE) at all applied potentials (without IR correction). Moreover, there were no liquid products as confirmed by ¹H-NMR spectra. We first performed linear scanning voltammetry (LSV) for the three catalysts (Fig. 3a). **Au₁₁/CNTs** show much higher current density and a more positive onset potential in CO₂ saturated 0.5 M KHCO₃ aqueous solutions than in N₂ purged aqueous solutions, indicating higher CO₂ reduction selectivity. **Au₄/CNTs** have similar onset potential and current density in both solutions, and did not exhibit high CO₂ reduction selectivity. This implies that the HER rather than the eCO₂RR is the main reduction process of the three catalysts. Interestingly, **Au(ı)P/CNTs** exhibit more positive onset potential and higher current density in CO₂ saturated 0.5 M KHCO₃ aqueous solution than in N₂ purged aqueous solution, suggesting some CO₂ reduction selectivity. Thus, the eCO₂RR catalytic activity can be arranged in descending order as **Au₁₁ > Au(ı)P > Au₄**, which are not simply related to the size of the clusters. Furthermore, electrochemical impedance spectroscopy (EIS) was carried out to investigate the electron transport properties of these catalysts at the electrode/electrolyte interface (Fig. 3b). These three samples had significantly different
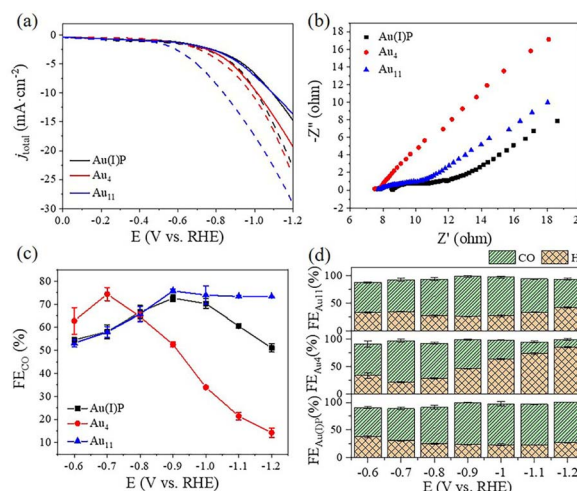

Fig. 3 The electrocatalytic performance of **Au(ı)P**, **Au₄** and **Au₁₁** in the eCO₂RR. (a) LSV curves of the three catalysts in an N₂-saturated (dotted line) and a CO₂-saturated (full line) 0.5 M KHCO₃ solution. (b) EIS and (c) FE_{CO} of the three catalysts. (d) Selectivity for various eCO₂RR products (CO vs. H₂) obtained on **Au₁₁**, **Au₄**, and **Au(ı)P**. The error bars represent the standard deviation of three tests at the same test potential.

electrochemical impedances, indicating different electron transport capabilities. The interface charge transfer rate was highest for **Au$_4$**, followed by **Au$_{11}$** and **Au(ɪ)P**. This suggests that **Au$_4$** would donate electrons to the intermediates more efficiently than **Au$_{11}$** and **Au(ɪ)P** during the electroreduction. As shown in Fig. 3c, **Au(ɪ)P/CNTs** and **Au$_{11}$/CNTs** show excellent selectivity for CO at all tested potentials, with CO faradaic efficiency (FE$_{CO}$) more than 50% at all test potentials. Specifically, **Au$_{11}$/CNTs** exhibit higher selectivity for CO with the highest FE$_{CO}$ (75.8% at -0.9 V vs. RHE) than **Au(ɪ)P/CNTs** (FE$_{CO}$: 72.6% at -0.9 V vs. RHE). Furthermore, the selectivity (HER vs. eCO$_2$RR) is shown in Fig. 3d. **Au$_{11}$/CNTs** show higher CO selectivity than **Au(ɪ)P/CNTs** from -0.9 to -1.2 V vs. RHE. This is due to the electron effect, indicating that clusters with free electrons is more favourable than the Au(ɪ) complex for selective reduction of CO$_2$ to CO. In contrast, **Au$_4$/CNTs** exhibit selectivity for CO at more positive potentials, while the hydrogen evolution reaction dominates over the eCO$_2$RR as the potential becomes more negative. The FE$_{CO}$ of **Au$_4$/CNTs** is 62.8% at -0.6 V vs. RHE with the highest FE$_{CO}$ of 74.3% at -0.7 V vs. RHE, suggesting that **Au$_4$/CNTs** have a smaller eCO$_2$RR overpotential than the other two catalysts. Note that, although **Au$_4$** has two free electrons, the cluster surface does not expose as much active site metal as **Au$_{11}$**. Moreover, H$_2$ is a competitive reaction product, and at a more negative applied potential, **Au$_4$/CNTs** exhibit a higher selectivity for H$_2$ (FE$_{H_2}$: 85.8% at -1.2 V vs. RHE) than **Au(ɪ)P/CNTs** (FE$_{H_2}$: 48.9%) and **Au$_{11}$/CNTs** (FE$_{H_2}$: 26.7%).

The CO partial current density (j_{CO}) increased with increasing applied potential for the three electrocatalysts (Fig. 4a). However, **Au$_4$/CNTs** show a slightly higher j_{CO} (1.8 mA cm^{-2}) than **Au$_{11}$/CNTs** (0.7 mA cm^{-2}) and **Au(ɪ)P/CNTs** (1.0 mA cm^{-2}) at -0.6 V vs. RHE. Furthermore, the j_{H_2} value of **Au$_4$/CNTs** increased more sharply than that of **Au$_{11}$/CNTs** (6.0 mA cm^{-2}) and **Au(ɪ)P/CNTs** (9.8 mA cm^{-2}) as the potential became more

negative (Fig. 4b). The electrochemically active surface area (ECSA) was measured to further reveal the reason for the difference in the catalytic performance of the three catalysts in the eCO$_2$RR. We recorded the current density of **Au(ɪ)P/CNTs**, **Au$_4$/CNTs** and **Au$_{11}$/CNTs** at different scan rates ranging from 0.02 to 0.1 V s^{-1} (Fig. S4†). We evaluated the double-layer capacitance (C_{dl}) of the three catalysts to be 0.648, 1.154 and 0.99 mF, respectively (Fig. 4c). And the ECSA of **Au(ɪ)P/CNTs**, **Au$_4$/CNTs** and **Au$_{11}$/CNTs** was calculated to be 16.20, 30.25 and 24.75 cm^2, respectively. Therefore, active surface area of the three catalysts can be arranged in descending order as **Au$_4$**> **Au$_{11}$**> **Au(ɪ)P**. Electrokinetic studies of CO$_2$ electroreduction were performed on these clusters to identify the origin of the eCO$_2$RR activities of the three Au-based catalysts. The Tafel plots were then recorded to analyse the reaction kinetics, where the Tafel slopes are calculated to be 448 mV dec^{-1}, 480 mV dec^{-1} and 422 mV dec^{-1} for **Au(ɪ)P/CNTs**, **Au$_4$/CNTs** and **Au$_{11}$/CNTs**, respectively (Fig. 4d). The High Tafel slopes of ca. 400 mV dec^{-1} of the three catalysts suggest that the first electron transfer step is the eCO$_2$RR rate-determining step. Furthermore, using the fingerprint absorbance peak (422 nm for **Au$_4$**; 419 nm for **Au$_{11}$**) as the metric, the absorbance change can be used as an indicator of the catalyst stability (Fig. S6†). Notably, the entire absorbance feature of **Au$_4$** and **Au$_{11}$** remains constant, though the intensity of the characteristic peaks of **Au$_4$** is drastically decreased, indicating that the structure of **Au$_4$** is difficult to maintain during the electroreduction.

Discussion on structure and electronic effects of the catalysts toward the eCO$_2$RR

Based on the experimental test results of the three catalysts for the eCO$_2$RR, we would like to discuss the effect of free electrons and stability of the three clusters toward the eCO$_2$RR. Note that, **Au(ɪ)P** and **Au$_{11}$** can convert CO$_2$ to CO with FE$_{CO}$ > 50% at all test potentials, suggesting that the +1 valence Au is the catalytically active site. However, cationic gold is quite oxidizing (Au$^{+/0}$ = 1.83 V), indicating that the Au(ɪ) complex was reduced into small particles by Au–P bond breaking during electroreduction. Therefore, as the reduction potential becomes negative, **Au(ɪ)P** becomes less selective for CO. Although **Au$_4$** contains +1 valence Au atoms, its Au(ɪ)/Au(0) ratio (**Au$_4$** : **Au$_{11}$** = 2 : 3) is less than that of **Au$_{11}$**, resulting in the highest FE$_{CO}$ (74.3%) of **Au$_4$** being slightly less than that of **Au$_{11}$** (FE$_{CO}$: 75.8%). However, as the particle size decreases, the adsorption capacity of H increases greatly. That means, for **Au$_4$**, the HER process became dominant at more negative potentials.

Conclusions

In conclusion, the smallest superatom with free electrons of Au$_4$(PPh$_3$)I$_2$ is synthesized by a one-pot method, and the **Au$_4$** tetrahedron could be considered as the smallest unit constituting the **Au$_{11}$** core. Moreover, **Au(ɪ)P**, **Au$_4$** and **Au$_{11}$** exhibited drastically different catalytic performances toward the eCO$_2$RR. **Au(ɪ)P** and **Au$_{11}$** could convert CO$_2$ into CO at all tested potentials with high FE$_{CO}$ (>50%). In contrast, **Au$_4$** can exclusively
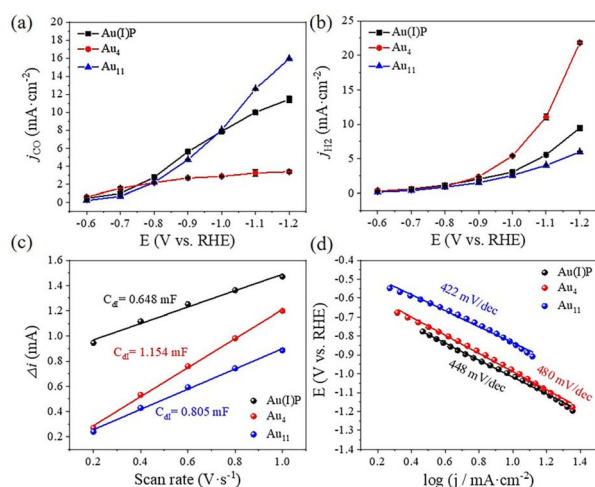

Fig. 4 (a) CO and (b) H$_2$ partial current density of **Au(ɪ)P**, **Au$_4$** and **Au$_{11}$** at different potentials. (c) The corresponding linear curves of current density and the scan rate (C_{dl}) for the three catalysts. (d) Tafel plots constructed for the eCO$_2$RR on the three catalysts in the 0.5 M KHCO$_3$ solution.

convert CO_2 into CO at more positive potentials, and as the potential becomes more negative, H_2 is the main product. According to structure analysis, the **Au$_4$** tetrahedron could not remain stable at more negative reduction potentials, resulting in decomposition and aggregation, which is the reason for the decay of catalytic performance of Au based catalysts towards the eCO_2RR. Moreover, Au(I) sites on the surface of the cluster were the active sites. This work provides an example at the atomic level to construct a structure–activity relationship between the structure and electroreduction of CO_2 of Au based catalysts.

Author contributions

S. W., Z. Y. and X. M. guided the whole experiment and conceived the idea. C. Z. conducted most of the experiments. M. D. and X. M. gave some advice for the characterization and analysis. S. W., Z. Y. and X. M. provided the funding support, and all the authors contributed to the final polishing of the manuscript.

Conflicts of interest

There are no conflicts to declare.

Acknowledgements

Notes and references

1 A. Wagner, C. D. Sahm and E. Reisner, *Nat. Catal.*, 2020, **3**, 775–786.
2 Y. Y. Birdja, E. Perez-Gallent, M. C. Figueiredo, A. J. Gottle, F. Calle-Vallejo and M. T. M. Koper, *Nat. Energy*, 2019, **4**, 732–745.
3 X. Y. Wang, Q. D. Zhao, B. Yang, Z. J. Li, Z. Bo, K. H. Lam, N. M. Adli, L. C. Lei, Z. H. Wen, G. Wu and Y. Hou, *J. Mater. Chem. A*, 2019, **7**, 25191–25202.
4 G. Wang, J. Chen, Y. Ding, P. Cai, L. Yi, Y. Li, C. Tu, Y. Hou, Z. Wen and L. Dai, *Chem. Soc. Rev.*, 2021, **50**, 4993–5061.
5 Y. T. Liu, D. H. Deng and X. H. Bao, *Chem*, 2020, **6**, 2497–2514.
6 P. De Luna, C. Hahn, D. Higgins, S. A. Jaffer, T. F. Jaramillo and E. H. Sargent, *Science*, 2020, **367**, eabb0992.
7 S. Nitopi, E. Bertheussen, S. B. Scott, X. Liu, A. K. Engstfeld, S. Horch, B. Seger, I. E. L. Stephens, K. Chan, C. Hahn, J. K. Norskov, T. F. Jaramillo and I. Chorkendorff, *Chem. Rev.*, 2019, **119**, 7610–7672.
8 Y. Zou and S. Wang, *Adv. Sci.*, 2021, **8**, 2003579.
9 M. B. Ross, P. De Luna, Y. F. Li, C. T. Dinh, D. Kim, P. Yang and E. H. Sargent, *Nat. Catal.*, 2019, **2**, 648–658.
10 M. Ding, L. Tang, X. Ma, C. Song and S. Wang, *Commun. Chem.*, 2022, **5**, 172.
11 Y. Li, H. K. Kim, R. D. McGillicuddy, S. L. Zheng, K. J. Anderton, G. J. Stec, J. Lee, D. Cui and J. A. Mason, *J. Am. Chem. Soc.*, 2023, **145**, 9304–9312.
12 Y. Li, M. Zhou, Y. Song, T. Higaki, H. Wang and R. Jin, *Nature*, 2021, **594**, 380–384.
13 S. Zhao, N. Austin, M. Li, Y. B. Song, S. D. House, S. Bernhard, J. C. Yang, G. Mpourmpakis and R. C. Jin, *ACS Catal.*, 2018, **8**, 4996–5001.
14 S. Li, A. V. Nagarajan, Y. Li, D. R. Kauffman, G. Mpourmpakis and R. Jin, *Nanoscale*, 2021, **13**, 2333–2337.
15 S. Li, D. Alfonso, A. V. Nagarajan, S. D. House, J. C. Yang, D. R. Kauffman, G. Mpourmpakis and R. Jin, *ACS Catal.*, 2020, **10**, 12011–12016.
16 S. Li, A. V. Nagarajan, D. R. Alfonso, M. Sun, D. R. Kauffman, G. Mpourmpakis and R. Jin, *Angew. Chem., Int. Ed.*, 2021, **60**, 6351–6356.
17 D. R. Alfonso, D. Kauffman and C. Matranga, *J. Chem. Phys.*, 2016, **144**, 184705.
18 N. Austin, S. Zhao, J. R. McKone, R. Jin and G. Mpourmpakis, *Catal. Sci. Technol.*, 2018, **8**, 3795–3805.
19 H. Seong, V. Efremov, G. Park, H. Kim, J. S. Yoo and D. Lee, *Angew. Chem., Int. Ed.*, 2021, **60**, 14563–14570.
20 S. F. Yuan, R. L. He, X. S. Han, J. Q. Wang, Z. J. Guan and Q. M. Wang, *Angew. Chem., Int. Ed.*, 2021, **60**, 14345–14349.
21 X. K. Wan, J. Q. Wang and Q. M. Wang, *Angew. Chem., Int. Ed.*, 2021, **60**, 20748–20753.
22 S. Zhuang, D. Chen, L. Liao, Y. Zhao, N. Xia, W. Zhang, C. Wang, J. Yang and Z. Wu, *Angew. Chem., Int. Ed.*, 2020, **59**, 3073–3077.
23 Y. N. Sun, X. Liu, K. Xiao, Y. Zhu and M. Y. Chen, *ACS Catal.*, 2021, **11**, 11551–11560.
24 J. Y. Xu, L. Xiong, X. Cai, S. S. Tang, A. C. Tang, X. Liu, Y. Pei and Y. Zhu, *Chem. Sci.*, 2022, **13**, 2778–2782.
25 L. C. McKenzie, T. O. Zaikova and J. E. Hutchison, *J. Am. Chem. Soc.*, 2014, **136**, 13426–13435.
26 A. K. Das, S. Mukherjee, S. S. R, A. S. Nair, S. Bhandary, D. Chopra, D. Sanyal, B. Pathak and S. Mandal, *ACS Nano*, 2020, **14**, 16681–16688.
27 C. C. McCrory, S. Jung, J. C. Peters and T. F. Jaramillo, *J. Am. Chem. Soc.*, 2013, **135**, 16977–16987.
28 C. Zeng, Y. Chen, G. Li and R. Jin, *Chem. Commun.*, 2014, **50**, 55–57.

© 2023 The Author(s). Published by the Royal Society of Chemistry